Biosensors and Bioelectronics 141 (2019) 111478

Contents lists available at ScienceDirect

Biosensors and Bioelectronics

journal homepage: www.elsevier.com/locate/bios

Nanoplasmonics-enhanced label-free imaging of endothelial cell monolayer integrity

Frederic A. Banville[a,b,c], Julien Moreau[c], Kevin Chabot[a,b], Andrea Cattoni[d], Ulrike Fröhlich[e], Jean-François Bryche[a,b], Stéphane Collin[d], Paul G. Charette[a,b], Michel Grandbois[a,e], Michael Canva[a,b,c,*]

[a] Laboratoire Nanotechnologies Nanosystèmes (LN2), CNRS UMI-3463, Université de Sherbrooke, Sherbrooke, J1K 0A5, Canada
[b] Institut Interdisciplinaire d'Innovation Technologique (3IT), Université de Sherbrooke, Sherbrooke, J1K 0A5, Canada
[c] Laboratoire Charles Fabry (LCF), Institut d'Optique Graduate School, Université Paris-Saclay, CNRS, Palaiseau, 91127, France
[d] Centre de Nanosciences et de Nanotechnologies (C2N), CNRS UMR-9001, Université Paris-Sud/Paris-Saclay, Palaiseau, 91120, France
[e] Département de Pharmacologie et Physiologie, Institut de Pharmacologie de Sherbrooke (IPS), Université de Sherbrooke, Canada

ARTICLE INFO

Keywords:
Label-free microscopy
Cell-based biosensing
Cell signaling
Endothelium
Nanostructured surface
Plasmonics
Spatial resolution

ABSTRACT

Surface plasmon resonance imaging (SPRI) is a powerful label-free imaging modality for the analysis of morphological dynamics in cell monolayers. However, classical plasmonic imaging systems have relatively poor spatial resolution along one axis due to the plasmon mode attenuation distance (tens of μm, typically), which significantly limits their ability to resolve subcellular structures. We address this limitation by adding an array of nanostructures onto the metal sensing surface (25 nm thick, 200 nm width, 400 nm period grating) to couple localized plasmons with propagating plasmons, thereby reducing attenuation length and commensurately increasing spatial imaging resolution, without significant loss of sensitivity or image contrast. In this work, experimental results obtained with both conventional unstructured and nanostructured gold film SPRI sensor chips show a clear gain in spatial resolution achieved with surface nanostructuring. The work demonstrates the ability of the nanostructured SPRI chips to resolve fine morphological detail (intercellular gaps) in experiments monitoring changes in endothelial cell monolayer integrity following the activation of the cell surface protease-activated receptor 1 (PAR1) by thrombin. In particular, the nanostructured chips reveal the persistence of small intercellular gaps ($< 5\,\mu m^2$) well after apparent recovery of cell monolayer integrity as determined by conventional unstructured surface based SPRI. This new high spatial resolution plasmonic imaging technique uses low-cost and reusable patterned substrates and is likely to find applications in cell biology and pharmacology by allowing label-free quantification of minute cell morphological activities associated with receptor dependent intracellular signaling activity.

1. Introduction

Investigating the interactions and responses of eukaryotic cells to external stimuli such as toxins, pathogens and hormones is instrumental in cell biology and for the development of new drugs. Cells have a large number of membrane-bound receptors that are essential to their metabolisms and functional activities. In particular, G-protein-coupled receptors (GPCRs), such as the PAR1 receptor of thrombin, compose the largest family of such receptors. The screening and monitoring of GPCRs signaling in cell-based assays have shown tremendous potential in the drug discovery process (Fang et al., 2008; Scott and Peters, 2010).

In recent years, the development and validation of biosensors modalities exploiting whole live cells as sensing elements have proven to be efficient methods for the analysis of receptor-dependent signaling activity. Most commonly used techniques employ fluorescent probes to specifically mark structures and molecular targets, as it is the case for total internal reflection fluorescence (TIRF) and surface plasmon enhanced fluorescence (SPEF) (Chabot et al., 2013; Goedhart and Gadella, 2009; He et al., 2009; Liebermann and Knoll, 2000; Ni et al., 2018). However, while being highly specific techniques, the use of labelling may impact the cells (Progatzky et al., 2013), which is not the case for non-invasive label-free methods (Bourassa et al., 2015; Bousse, 1996; Chabot et al., 2009; Fang, 2011; Pancrazio et al., 1999). Cell activity

* Corresponding author. Laboratoire Nanotechnologies Nanosystèmes (LN2), CNRS UMI-3463, Université de Sherbrooke, Sherbrooke, J1K 0A5, Canada.
E-mail address: michael.canva@usherbrooke.ca (M. Canva).

https://doi.org/10.1016/j.bios.2019.111478
Received 25 March 2019; Received in revised form 21 June 2019; Accepted 24 June 2019
Available online 25 June 2019
0956-5663/

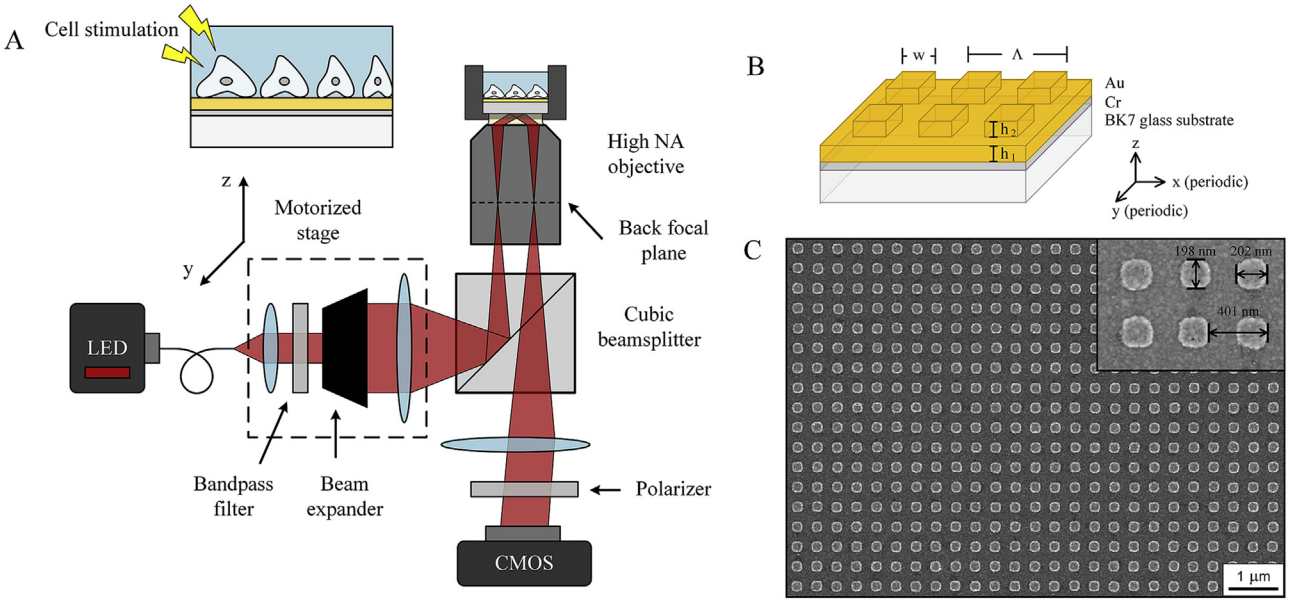

Fig. 1. *Nanostructured chips used in live-cell SPR imaging.* A) Schematic of the optical system based on a high numerical aperture microscope objective; B) Schematic of the SPRI chip: BK7 glass substrate – Cr adhesion film (3 nm) – flat or nanostructured Au films. The flat film is composed of a uniform film (height of h_1), while the nanostructured film is composed of a uniform film (height of h_1) and a grating (height of h_2, width of w and period of Λ) periodic along x and y axes; C) SEM image of nanostructured sample fabricated by soft UV-NIL with inset showing high fabrication resolution in terms of structure shape and grating dimensions ($h_1 = h_2 = 25$ nm, $w = 200$ nm, $\Lambda = 400$ nm).

has been successfully monitored using several label-free biosensing methods, in particular by electrochemical impedance spectroscopy (Giaever and Keese, 1993; McGuiness, 2007), resonant Waveguide Grating (Fang et al., 2006; Ferrie et al., 2010), surface plasmon resonance (Chabot et al., 2013, 2012; 2009; Giebel et al., 1999; Maltais et al., 2012; Peterson et al., 2009; Wang et al., 2012) and metal-clad waveguides (Söllradl et al., 2018b, 2018a, 2017). Evanescent-field based methods such as surface plasmon resonance (SPR) and metal-clad waveguides (MCWG) are highly sensitive to small variations in refractive index at the sensor surface (hundred of nanometers). This selectivity in volume can be especially useful when studying cell-substrate interactions such as cell adhesion to the surface (Howe et al., 2019; Kreysing et al., 2018; Peterson et al., 2018; Son et al., 2017; Toma et al., 2014; Watanabe et al., 2012) and changes in a cell monolayer integrity (Cuerrier et al., 2008; Söllradl et al., 2018a).

SPR imaging (SPRI) has been used to spatially resolve individual cells and subcellular structures (Peterson et al., 2014). However, SPRI is limited in spatial resolution due to the mode attenuation distance, which results in a directional blur in acquired images that was described by analytical models (Berger et al., 1994; Yeatman, 1996). Various approaches have been proposed to address this issue, but carry losses in sensitivity, temporal resolution or image contrast (Banville et al., 2015; Berguiga et al., 2016; de Bruijn et al., 1993; Giebel et al., 1999; Huang et al., 2007; Somekh et al., 2000; Wei et al., 2015). In previous works, we showed that nanostructured metal films are well suited for high resolution SPRI as they support a "hybrid" plasmonic mode, which is the result of a strong coupling between propagating (SPP) and localized (LSP) modes (Sarkar et al., 2015). This hybrid mode benefits from a reduction in mode attenuation distance due to the localized mode properties. In a previous manuscript by our group (Banville et al., 2018), we demonstrated that the nanostructured film geometry can be designed in such a way as to improve spatial resolution while mitigating imaging performance losses. We showed that a trade-off between the attenuation length and the sensitivity is required, while maintaining a high image contrast. The numerical analysis of the nanostructured film geometry confirmed that the improvements in spatial resolution derives from the decrease in the uniform gold film thickness, while the high contrast is rather associated to the presence of the nanostructures. In this previous work, we have identified an optimal nanostructured film geometry (grating of 25 nm thick, 200 nm width and 400 nm period on a 25 nm Au film) that was applied to the design of our nanostructured chips proposed in the current manuscript. The performances were compared to those of "conventional" SPR sensor chips (50 nm continuous Au film), and experimental results showed a significant decrease in attenuation length while maintaining high image contrast in SPR imaging, where features as small as 1 µm wide could be resolved in all dimensions.

Quantitative high spatial resolution imaging is of particular interest in label-free studies of cell monolayer permeability. Indeed, most commonly used techniques employ fluorescent markers to spatially track intercellular gap formation and associated changes in cell monolayer integrity. Earlier published work from our group based on MCWG imaging showed that intercellular gaps in endothelial cell monolayers can be resolved in a label-free manner (Söllradl et al., 2018a). However, only "large" gaps (radius $>$ 4 µm) were resolved as the spatial resolution limit of the MCWG system was 5 µm and smaller gaps could not be resolved.

In this study, we used nanostructured metal surfaces as a method to increase spatial resolution in SPRI and thus to improve the performance of this imaging modality to quantify morphological changes in an endothelial cell layer exposed to permeability enhancing agents. We fabricated the nanostructured metal surfaces by low-cost and large surface area Soft Nanoimprint lithography and we showed multiple reuse of the same substrate without degradation of its functionality. We demonstrated that surface nanostructuring, by enhancing spatial resolution in SPRI, also enhances measurement sensitivity of cell activity by improving detection of reversible intercellular gap formation in the cell layer.

2. Materials and methods

2.1. Sensor chip design

The imaging system setup presented in Fig. 1A is based on a high numerical aperture microscope objective and has previously been described (Söllradl et al., 2017). The excitation light (LED filtered at

830 nm, FWHM of 10 nm) is focused on the back focal plane of the objective (NA = 1.46), reflected by the sensor chip placed atop the objective, and imaged by a CMOS camera. The light incident on the sensor chip is collimated and the incidence angle is chosen for maximum mode coupling by moving the focal point in the back focal plane of the objective with the motorized stage along y-z axes.

The sensor chip metal surface nanostructure geometry (Fig. 1B) was designed numerically as explained elsewhere (Banville et al., 2018) to achieve the optimal compromise between spatial resolution limited by the mode attenuation length, image contrast and sensitivity. The chips are composed of a BK7 glass cover slip (170 µm thick, 22 × 22 mm, Fisher Scientific), a 3 nm Cr adhesion layer, a 25 nm continuous Au film (h_1), 25 nm thick (h_2) square Au nanostructures (width w of 200 nm, grating period Λ of 400 nm). They were fabricated by lift-off of gold using soft UV nanoimprint lithography (soft UV-NIL) over a surface area of 1 cm^2. This technique uses cheap and flexible polydimethylsiloxane (PDMS) based stamps (hard-PDMS/PDMS) replicated from a Si master fabricated by electron beam lithography and dry etching. Since the PDMS based stamp can be used tens of time, this technology offers fast large-scale patterning at low cost compared to electron beam lithography (Cattoni et al., 2011a, 2011b). Fig. 1C shows SEM images of a nanostructured chip fabricated with high resolution on a large scale (grating surface of 1 cm^2).

The unstructured sensor chips used for reference had a 50 nm continuous Au layer (BK7 glass cover slip, 3 nm Cr adhesion layer) as most commonly used in SPR biosensing. A layer of cells was grown on the sensor surfaces in a biological medium. As cells are much larger (> 10 µm) than the grating dimensions, they completely cover nanostructures. Optical coupling conditions were chosen to obtain a reflectance minimum (maximum coupling to the SPR mode) in areas without cells. This results in cells appearing as bright objects in the SPRI images and areas devoid of cells appearing as dark regions as can be seen in Fig. 2. The round oscillatory patterns visible in SPRI images do not correspond to biological structures at the metal surface, but rather to coherence artifacts due to dust particles in the optical path. All SPRI images in this work are presented with the same grayscale range.

Fig. 2 shows glioblastoma cells (U-373 GM) imaged with brightfield along with unstructured and nanostructured surface SPRI chips. Cells imaged on the structured film (B) are better resolved than on the unstructured film (A), while maintaining a high image contrast as shown in (C). In a previous work (Banville et al., 2018), we showed by numerical modeling and confirmed experimentally that the attenuation length for a 50 nm unstructured Au film is ~11 µm and ~1.7 µm for the proposed nanostructured film. This reduction in attenuation length improves the spatial resolution, which results in gaps between cells and cell edges being more defined on the nanostructured sensor chip, the plasmonic mode allowing to isolate the structural parts in the immediate vicinity (~100 nm) of the surface.

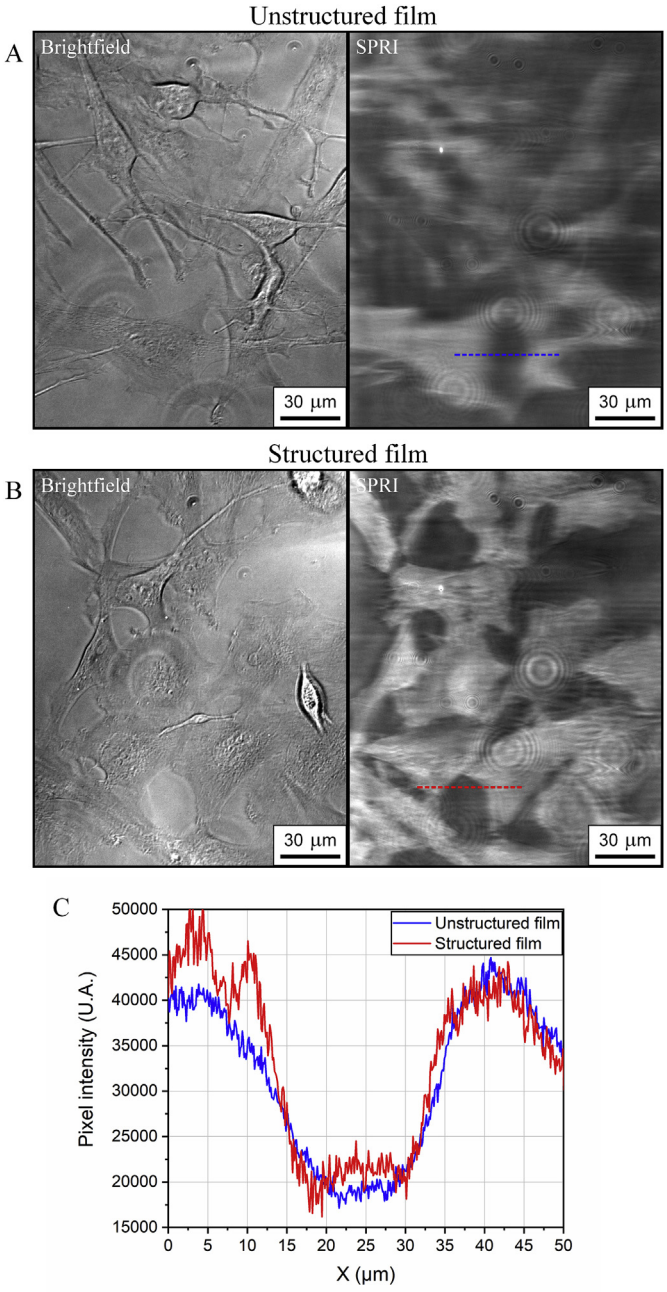

Fig. 2. *Surface nanostructuring impact on SPR cell imaging.* A) Brightfield and reflectance images (λ = 830 nm) of glioblastoma cells (U-373 GM) atop an unstructured gold film (50 nm); B) Brightfield and reflectance images of glioblastoma cells atop the nanostructured gold film (25 nm continuous film, 25 nm thick nanostructures, width of 200 nm, grating period of 400 nm); C) Line profiles of SPRI images showing better resolved cell edges for the structured film. (For interpretation of the references to colour in this figure legend, the reader is referred to the Web version of this article.)

2.2. Cell culture and reagents

Two cell types were used: glioblastoma cell line U-373 GM (ATCC, Manassas, USA) and an immortalized endothelial cell line EA.hy 926 (kindly provided by Dr. CJ Edgell, University of North Carolina, USA). The two cell types served respectively to qualitatively and to quantitatively investigate the impact of surface nanostructuring on cell activity studies through improved spatial resolution. Cells were maintained in EME (U-373 GM) or DMEM (EA.hy 926) supplemented with 10% temperature inactivated FBS, 2 mM L-glutamine, 50 IU/ml penicillin and 50 g/ml streptomycin at 37 °C in a 5% CO_2 incubator on 100 mm diameter tissue culture Petri dishes (Corning) and were subcultured upon reaching 70–80% confluence using Trypsin/EDTA (0.25%), within approximately three days.

Both types of sensor chips (unstructured and nanostructured surfaces) were seeded with ~1.5×10^5 cells (U-373 GM) or ~2.5×10^5 cells (EA.hy 926) directly atop the uncoated ethanol-sterilized Au film. U-373 GM were grown to ~50% confluence in two days, while EA.hy 926 were grown to full confluence within seven days. The presence of a nanoscale surface grating was not found to affect the growth rate nor the morphology of the cells.

Prior to the experiments, the sensor chips were washed twice in HEPES-Buffered Salt Solution (HBSS) heated at 37 °C, then mounted in our custom sample holder, maintained at 37 °C (TC1-100, Bioscience Tools). Cells were kept in the HBSS buffer solution for an hour to stabilize on the imaging system prior to measurements. An optimal plasmon coupling angle was identified by scanning angularly the

incident light for maximal image contrast between the cell layer and the surrounding areas devoid of cells. This coupling angle was kept fixed throughout the image sequence acquisition.

LPS stimulation (Lipopolysaccharide, Sigma-Aldrich, 0.5 mg/ml solution) was used for the estimation of the threshold for intercellular gap detection, described in the following section, while thrombin was used to disrupt reversibly the monolayer (Sigma-Aldrich, 5 and 10 nM solutions), thus mimicking biological conditions of modulation in cell monolayer permeability. The sensor chips were cleaned with soap, distilled water, ethanol and dried with N_2 at the end of each experiments. The nanostructured chips were reused multiple times (over 50 times each) in the course of our studies, for static observation of individual cells and dynamic monitoring of cell activity in confluent cell populations, without significant performance deterioration. To qualify this stability, we have checked that the incident light angle for maximum plasmonic coupling did not significantly drift during the several months of experiments, which would have been evident if any degradation of the nanostructured metal surface had occurred. Their low-cost and reusability validate their reliability and usefulness in practical use (see Fig. 1 in Appendix A for SEM images of the nanostructured sensor chip prior to initial use and after multiple reuses).

2.3. Threshold estimation for intercellular gap detection

The SPRI instrument image acquisition parameters were chosen to minimize background noise while maximizing pixel intensity dynamic range. SPRI images were generated at 10-s intervals by averaging three successive CMOS camera images, low-pass filtered for high-frequency noise reduction and normalized by subtracting a dark reference acquired at the beginning. The endothelial cell monolayer integrity disruption following stimulation was characterized by monitoring and analyzing the formation of intercellular gaps in the monolayer. To do so, the image pixels were segmented into two populations corresponding to the presence or absence of cells using an intensity-based thresholding algorithm (Otsu, 1979). The thresholding process was found to be robust owing to the high contrast in the SPRI images between cellular regions and intercellular gaps, allowing the characterizing of intercellular gap size distribution in any given image. The segmentation threshold pixel intensity values were determined from calibration experiments by stimulating a confluent layer of EAh926 cells with the cytotoxin LPS. In those experiments, the LPS stimulation lead to irreversible loss in the monolayer integrity, as can be seen in Fig. 3A (0 min and 100 min). These experiments allowed the acquisition of sequences of intensity distribution histograms spanning the range from full cell confluence to complete cell monolayer detachment. This shift between both populations was necessary to identify the intensity threshold defining them, which could not be accurately obtained in the thrombin experiment, which exhibit a partial and reversible cell layer response. Those threshold values were applied to all experiments (one for each sensor chip type, unstructured and nanostructured) by conserving the acquisition parameters and sensor chip geometries.

Three images from a sequence acquired during a typical calibration experiment on nanostructured film are shown in Fig. 3A (T = 0 min, 57 min, 100 min) with their associated histograms (Fig. 3B). The two threshold values were calculated from the image in each of the two corresponding calibration sequences where the cell surface coverage was approximately 50%. Pixel intensity histograms for such images had a wide distribution (large full-width at half maximum, FWHM) with a relatively low pixel count at maximum (dotted curve in Fig. 3B), compared to the histograms for images of full confluence (plain curve in Fig. 3B) and full detachment (dashed curve in Fig. 3B). Fig. 3C presents the evolution over time of the image histogram maximum values (blue curve) and of the image histogram FWHM (red curve). The two 50% confluence images were selected automatically from the calibration data shown in Fig. 3C at the point where the histogram FWHM was largest and pixel count at maximum simultaneously lowest (dashed black line). The intensity-based thresholding algorithm was then applied to those images resulting in pixel intensity thresholds (dashed green vertical line in Fig. 3B) for the nanostructured and unstructured films respectively of 29568 and 30208 (see Fig. 2 in Appendix A for the unstructured film pixel intensity threshold evaluation).

Thereafter, the sizes of the gaps in the endothelium cell layer were quantified by using connected-component labeling with the following sequence:

1) Gaussian-filtering to remove high-frequency noise (3 × 3 kernel) by using the OpenCV Python function *GaussianBlur()*.
2) Image binarization by automatic clustering-based thresholding using the OpenCV Python function *threshold()*.
3) Connected-component labeling using the scikit-image Python package functions: *label()* to connect regions in the binary images, *regionprops()* to measure the properties of the labeled image regions.
4) Statistical analysis of regions area.

Gap areas under 1 μm^2 were found to be highly dependent on image noise and were not considered in the statistical analyses. For visualization purposes, as shown for example in Fig. 4 below, gap contours were highlighted (yellow) in the images using the morphological transformation “gradient” with the Python function *morphologyEx()*.

3. Results and discussion

3.1. Monitoring of cell response in confluent endothelial cell monolayers

Cell responses following protease-activated receptor 1 (PAR1) activation by thrombin have been studied for its role in haemostasis and inflammation mechanisms (Coughlin, 2000). Thrombin has been extensively used to destabilize endothelial cell layers for instance to investigate its effect on barrier function permeability (Amado-Azevedo et al., 2018; Bae et al., 2009; Minami et al., 2004; O'Brien et al., 2000; Söllradl et al., 2018a; Troyanovsky et al., 2008; van der Heijden et al., 2011). Thrombin binds with the cell protease-activated receptor 1 (PAR1), activates intracellular signaling cascades which induces endothelial cell contraction, cell-cell molecular junction disassembly and the modulation of cell attachment onto the substrate (Opal and van der Poll, 2015). These events are associated to transient and reversible gap formation in the endothelial cell layer and have previously been reported (Rabiet et al., 1996; Vouret-Craviari et al., 1998). In these studies, the cytoskeleton was stained, in particular the F-actin with fluorescent-labeled phalloidin, and fluorescence images show that thrombin induces cytoskeletal reorganization resulting in the rounding of the endothelial cells (HUVECs and Ea.hy 926 cell lines), which forms intercellular gaps significantly increasing monolayer permeability.

To demonstrate the potential of nanostructured SPRI chips in label-free cell studies, EA.hy 926 endothelial cells were grown to confluence and stimulated with thrombin. Fig. 4A–B present the time sequence of SPRI images acquired during endothelial cell layer integrity disruption following thrombin stimulation (10 nM concentration). The intercellular gaps (dark zones selected as described in previous section) are outlined in yellow to facilitate visualization. Negative controls were performed prior to stimulation by injecting HBBS buffer solution and did not result in observable cell response. As shown in the image sequence, intercellular gaps become apparent at 8 min. Afterwards, the endothelial cells gradually recover to return to a quasi-confluent monolayer.

In the images, a larger number of small gaps are visible on the nanostructured film, while mainly fewer large gaps are seen on the unstructured film. This phenomenon is most likely a consequence of the lower spatial resolution when using an unstructured film where small gaps are either unobservable or combined with other gaps due to the blur in SPRI images in the direction of mode propagation (red arrows,

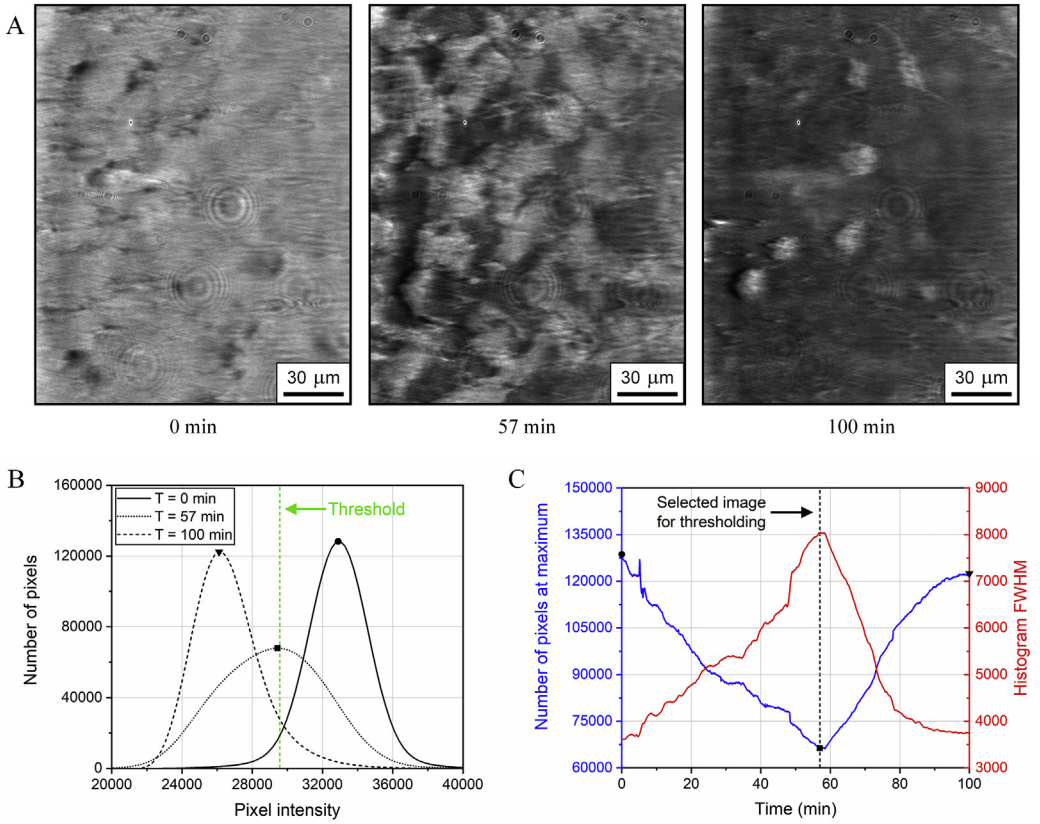

Fig. 3. *Threshold identification for intercellular gap detection: nanostructured metal films.* A) SPRI images (λ = 830 nm) of EA.hy 926 endothelial cells on a nanostructured Au film where the monolayer integrity is disrupted following LPS stimulation. At 0 min, the cell monolayer confluence is close to 100%. At 100 min, virtually no cells are visible on the sensor surface; B) Histograms of pixel intensity of three SPRI images taken at different times (0, 57 and 100 min). The green dashed line corresponds to the pixel intensity threshold calculated by automatic clustering-based thresholding from the image at 57 min; C) Evolution over time of histogram maximum value (blue) and FWHM (red). The image selected for the automatic clustering-based thresholding corresponds to the image where the FWHM is highest and the histogram maximum is lowest (black dashed line). The markers in (B) and (C) correspond to the maximum values in the pixel histograms at T = 0 min (circle), T = 57 min (square) and T = 100 min (triangle). (For interpretation of the references to colour in this figure legend, the reader is referred to the Web version of this article.)

from left to right). In addition, loss of information in gap morphology with the unstructured film is also noticeable by the smoothness of the edges and the preferential orientation of the gaps along the direction of mode propagation.

Two thrombin concentrations (red: 5 nM, black: 10 nM) were used to induce endothelial monolayer response in order to compare the effects on gap formation. The image data were analyzed in terms of the coverage percentage by the cell layer as a function of time as shown in Fig. 5. As expected, monolayer integrity is rapidly lost after stimulation and gradually recovers over time to return to a quasi-confluent layer, after 25–30 min (5 nM) and 40–45 min (10 nM).

It has been shown that nanostructures can have a significant impact on cellular phenotype, such as on cell adhesion, morphology, proliferation, migration, alignment, etc. (Skoog et al., 2018). However, studies have determined that nanostructures with heights inferior to 35 nm have little to no effect on cells and no observable phenotype changes have been recorded in such cases (Dalby et al., 2004; Loesberg et al., 2007). This is indeed the case for the proposed nanostructured surface, as shown in the brightfield images in Fig. 2 which shows no obvious impact of surface nanostructuring on the general morphology of cells, or in the time course of the cell response presented in Fig. 5, which shows similar responses profile for both sensor chip types following thrombin stimulation.

3.2. Quantification of intercellular gap morphology dynamics in endothelial cell monolayers

The complete sequence of images shown partially in Fig. 4 was analyzed to quantify gap concentration dynamics as a function of size upon thrombin stimulation for both unstructured and nanostructured sensor chips. The statistics were extracted from the data collected and quantified via the connected-component labeling process previously described. Fig. 6A–D show the total number of intercellular gaps in the images for both sensor chip types in four size ranges over time: 1–2 µm^2, 2–5 µm^2, 5–10 µm^2 and over 10 µm^2. For example, gap areas in the 1–2 µm^2 category correspond to zones having between 69 and 139 pixels, when considering an individual pixel surface area of 0.0144 µm^2 (0.120 µm × 0.120 µm). Gap areas under 1 µm^2 were not considered in the analyses as their labeling was assumed to be sensitive to image noise. As shown by the black line plots for the nanostructured film in Fig. 6A–D, intercellular gap formation is triggered by thrombin stimulation at 2.5 min and gaps rapidly develop until approximately 10 min, after which the endothelial cells start to recover. The number of gaps then decreases as the layer gradually returns to a quasi-confluent monolayer (light grey region) and there is a significant drop in larger gaps over 5 µm^2 after 40–45 min. The number of smaller gaps (1–5 µm^2) is high until around 80 min and then returns to the pre-stimulation baseline levels.

As shown in Fig. 6, the number of detected intercellular gaps under 10 µm^2 is significantly greater for the nanostructured film and the data

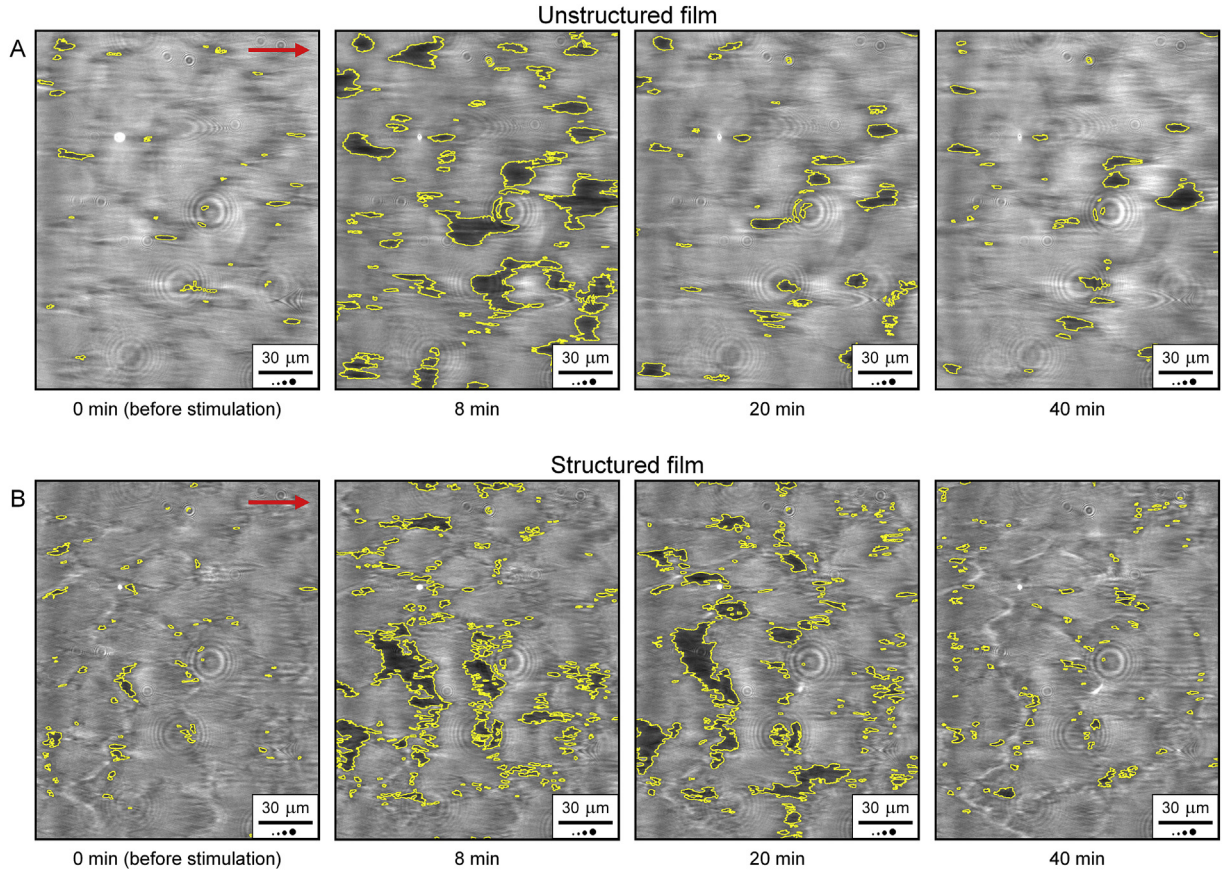

Fig. 4. *Endothelial cell layer activation by thrombin: gap formation monitoring.* Reflectance images (λ = 830 nm) of EA.hy 926 endothelial cells on unstructured (A) and structured (B) Au films before and after cell layer activation by thrombin stimulation (concentration of 10 nM). The images show the evolution of intercellular gaps outlined in yellow that appear after stimulation and gradually disappear until cell layer integrity is recovered. The direction of plasmon mode propagation is from left to right (red arrows). The nanostructured film images show a higher spatial resolution resulting in improved gap morphology measurement throughout the experiment. The circles in the legend represent equivalent gap pixel areas of 1, 2, 5 and 10 µm^2, respectively. (For interpretation of the references to colour in this figure legend, the reader is referred to the Web version of this article.)

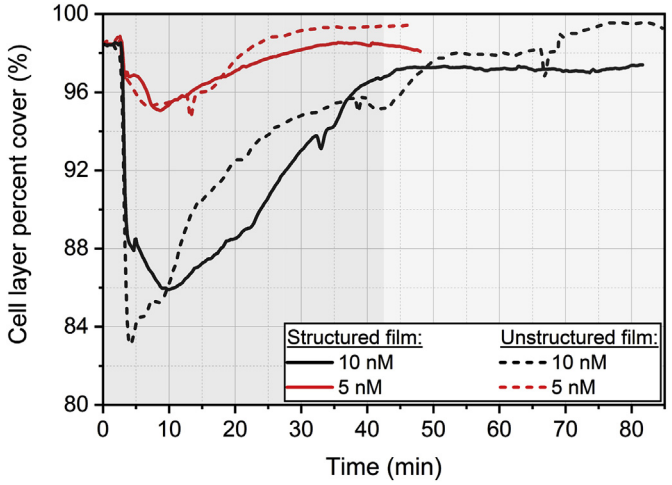

Fig. 5. *Endothelial cell layer activation by thrombin: monolayer confluence tracking.* Percent coverage of the endothelial cell layer as a function of time following stimulation with thrombin (black: 10 nM, red: 5 nM). The minimum in monolayer integrity occurs at 2.5 min after injection followed by full recovery at 40–45 min (light grey). The curves obtained from unstructured and nanostructured surface show similar response profiles and no observable phenotype changes due to the surface nanostructure are observed. (For interpretation of the references to colour in this figure legend, the reader is referred to the Web version of this article.)

shows much more variation over time owing to the higher spatial SPRI resolution. Conversely, in the data for the unstructured film, the total number of gaps under 10 µm^2 varies little over time. Interestingly, the nanostructured film data after 40–45 min for gaps below 5 µm^2 shows that the endothelial monolayer integrity takes much longer to recover than would otherwise be determined from the unstructured film data or from Fig. 5, which may be significant in terms of membrane permeability to small molecules. Indeed, the overall cell coverage dynamics presented in Fig. 5 are mainly governed by large gaps in the endothelial layer. For example, at the 8 min mark (Fig. 6E), the total surface of small intercellular gaps for the structured and unstructured films is respectively ~500 µm^2 and ~130 µm^2, while the total surface imaged is ~31000 µm^2. This corresponds to a respective drop in cell coverage of 1.6% and 0.4%, which is significantly smaller than the one registered in Fig. 5 (12% and 13%). Both analyses should then be viewed as complementary rather than conflicting.

Fig. 6E quantifies the impact of thrombin concentrations (0 nM, 5 nM and 10 nM) on gap dynamics for the two sensor chip types at the 8 min mark. For the unstructured film, the number of small gaps detected (< 10 µm^2) does not vary with thrombin concentration, and it is only for areas over 10 µm^2 that a significant number of gaps are quantified. This difference in detection is the result of smaller gaps combining into larger gaps due to the blurring effect associated with a longer attenuation length. This further supports the fact that gaps with sizes under that of the mode attenuation length cannot be detected accurately. Conversely, in the case of the nanostructured film, the cell layer response is quantifiable at lower concentration of thrombin

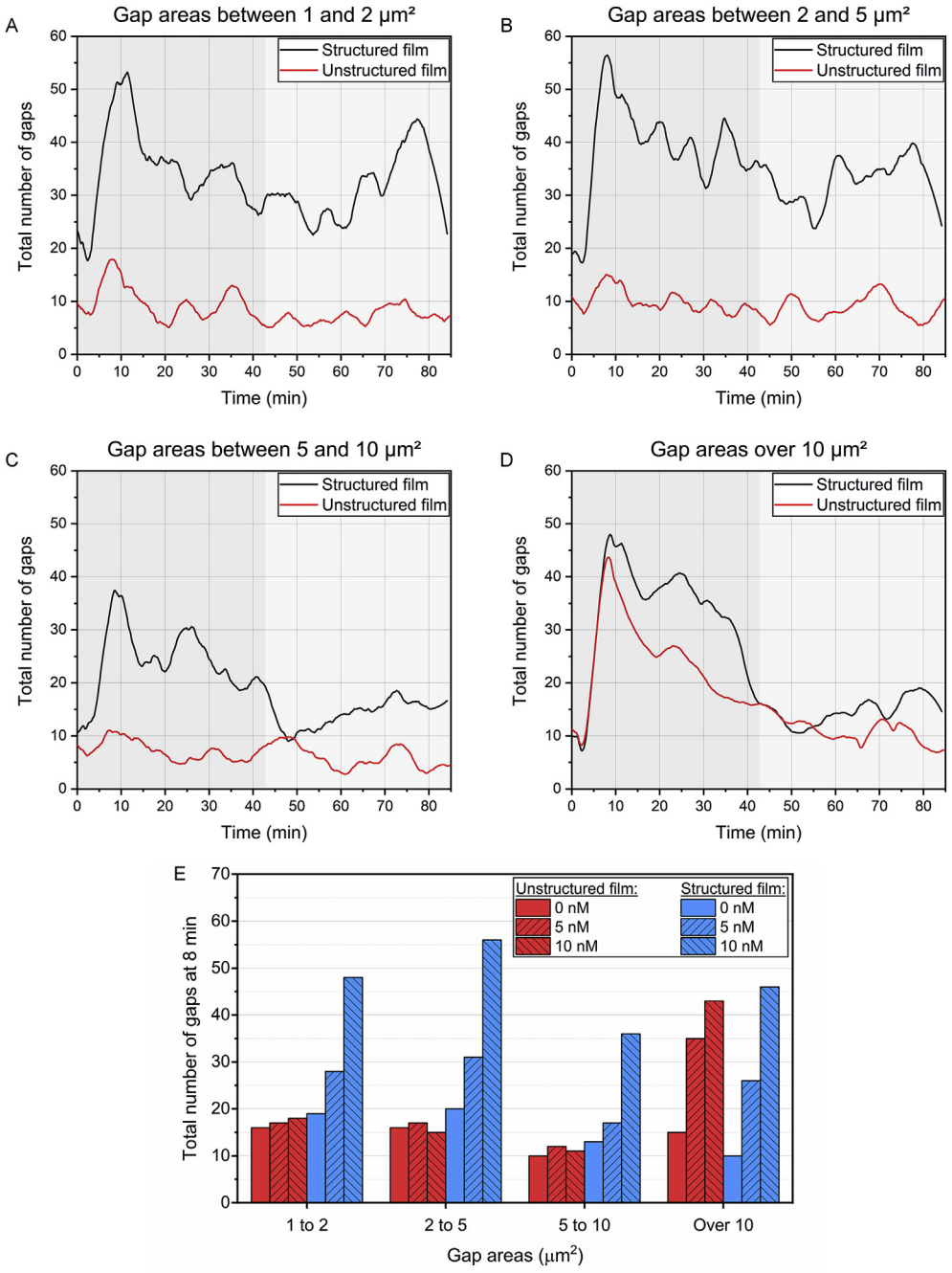

Fig. 6. *Quantification of intercellular gap morphology dynamics and effect of thrombin concentration.* Total number of gaps detected over time following 10 nM thrombin injection at 2.5 min with areas between 1 and 2 μm^2 (A), 2 and 5 μm^2 (B), 5 and 10 μm^2 (C) and over 10 μm^2 (D). Gaps with areas under 10 μm^2 are detected in greater numbers for the structured film (black) compared to the unstructured film (red); E) Intercellular gaps detected at 8 min for both sensor chip types at two thrombin concentrations (5 nM and 10 nM) and for no thrombin stimulation (0 nM). (For interpretation of the references to colour in this figure legend, the reader is referred to the Web version of this article.)

stimulation (5 nM), where significant numbers of gaps between 1 and 5 μm^2 are detected. Indeed, to the exception of gaps areas between 5 and 10 μm^2, the number of detected gaps is well above the baseline of 0 nM. Clearly, the ability of the nanostructured sensor chips to detect small gaps (1–5 μm^2) confers a strong ability to study cellular dynamics with SPRI such as endothelial cell layer activation by thrombin.

4. Conclusion

In this work, we demonstrated a novel surface imaging method for monitoring and quantifying cell surface activity by using the case of confluent endothelial cell monolayers. This was achieved by significantly improving the spatial resolution in SPRI systems by way of metal surface nanostructuring while preserving sensitivity and image contrast. Although still dependant on the mode attenuation length, micrographs of live cells obtained with the proposed nanostructured chips were found to have sharper and more defined edges. These nanostructured sensor chips were fabricated by low-cost Soft Nanoimprint lithography over a large surface area (1 cm^2), and were demonstrated to be reusable.

The performances of the proposed sensor chips for cell applications were evaluated by conducting experiments in which endothelial cell monolayers were stimulated with agents known to disrupt cell-cell junctions and cell-substrate adhesions. Specifically, thrombin was used to transiently and reversibly generate gaps in the endothelial layer while monitoring and quantifying their evolution over time. We demonstrated that the detection of intercellular gaps, ranging from 1 to 10 μm^2, is increased several folds throughout experiments when using a nanostructured metal film. This high sensitivity to low micrometer sized gaps detection provided by nanostructured biochip makes them well suited for label-free endothelial cell monolayer studies and should prove very useful for the monitoring of other subcellular features such

as cell focal adhesions. Further cell monolayer studies would benefit from exploiting our nanostructured sensor chips in labeled experiments, such as combining SPR and fluorescence imaging, where complementary data could be acquired simultaneously.

Declaration of interests

The authors declare that they have no known competing financial interests or personal relationships that could have appeared to influence the work reported in this paper.

CRediT authorship contribution statement

Frederic A. Banville: Conceptualization, Methodology, Software, Investigation, Visualization, Writing - original draft. **Julien Moreau:** Methodology, Supervision, Writing - original draft. **Kevin Chabot:** Data curation, Validation. **Andrea Cattoni:** Resources. **Ulrike Fröhlich:** Resources. **Jean-François Bryche:** Data curation, Validation. **Stéphane Collin:** Supervision. **Paul G. Charette:** Supervision, Writing - review & editing. **Michel Grandbois:** Supervision, Writing - review & editing. **Michael Canva:** Supervision, Writing - review & editing.

Acknowledgements

This work was supported by the Natural Sciences and Engineering Research Council of Canada with Discovery Grants for M.G. (2014-05930), M.C. and P.G.C (2015-05188), and by the Fonds de Recherche du Québec - Nature et Technologies for M.G. and P.G.C (2013PR168908). F.A.B. is supported by a doctoral scholarship from the FRQNT and by a French doctoral contract (MESRI) with the Université Paris-Saclay. LN2 is an international laboratory (Unité Mixte Internationale UMI 3463) jointly managed by French CNRS and the Université de Sherbrooke as well as Université de Lyon (ECL, INSA de Lyon, CPE) and the Université Grenoble Alpes (UGA). LN2 is associated to the French national nanofabrication network RENATECH and is also financially supported by FRQNT. The C2N work was partially supported by the French RENATECH network.

Appendix A. Supplementary data

Supplementary data to this article can be found online at https://doi.org/10.1016/j.bios.2019.111478.

References

Amado-Azevedo, J., de Menezes, R.X., van Nieuw Amerongen, G.P., van Hinsbergh, V.W.M., Hordijk, P.L., 2018. A functional siRNA screen identifies RhoGTPase-associated genes involved in thrombin-induced endothelial permeability. PLoS One 13, e0201231. https://doi.org/10.1371/journal.pone.0201231.

Bae, J.-S., Kim, Y., Park, M.-K., Rezaie, A.R., 2009. Concentration dependent dual effect of thrombin in endothelial cells via Par-1 and Pi3 Kinase. J. Cell. Physiol. 219, 744–751. https://doi.org/10.1002/jcp.21718.

Banville, F., Söllradl, T., Zermatten, P.-J., Grandbois, M., Charette, P.G., 2015. Improved resolution in SPR and MCWG microscopy by combining images acquired with distinct mode propagation directions. Opt. Lett. 40, 1165–1168.

Banville, F.A., Moreau, J., Sarkar, M., Besbes, M., Canva, M., Charette, P.G., 2018. Spatial resolution versus contrast trade-off enhancement in high-resolution surface plasmon resonance imaging (SPRI) by metal surface nanostructure design. Optic Express 26, 10616–10630. https://doi.org/10.1364/OE.26.010616.

Berger, C.E.H., Kooyman, R.P.H., Greve, J., 1994. Resolution in surface plasmon microscopy. Rev. Sci. Instrum. 65, 2829–2836. https://doi.org/10.1063/1.1144623.

Berguiga, L., Streppa, L., Boyer-Provera, E., Martinez-Torres, C., Schaeffer, L., Elezgaray, J., Arneodo, A., Argoul, F., 2016. Time-lapse scanning surface plasmon microscopy of living adherent cells with a radially polarized beam. Appl. Opt. 55, 1216–1227. https://doi.org/10.1364/AO.55.001216.

Bourassa, P., Söllradl, T., Maltais, J.-S., Charette, P.G., Gendron, L., Grandbois, M., 2015. Surface plasmon resonance to study cell signaling and GPCR functional selectivity in live cells. In: Fang, Y. (Ed.), Label-Free Biosensor Methods in Drug Discovery. Springer New York, New York, NY, pp. 183–195. https://doi.org/10.1007/978-1-4939-2617-6_10.

Bousse, L., 1996. Whole cell biosensors. Sensor. Actuator. B Chem. 34, 270–275. https://doi.org/10.1016/S0925-4005(96)01906-5.

Cattoni, A., Chen, J., Decanini, D., Shi, J., Haghiri-Gosnet, A.-M., 2011a. Soft UV nanoimprint lithography: a versatile tool for nanostructuration at the 20nm scale. In: Cui, B. (Ed.), Recent Advances in Nanofabrication Techniques and Applications. InTech. https://doi.org/10.5772/21874.

Cattoni, A., Ghenuche, P., Haghiri-Gosnet, A.-M., Decanini, D., Chen, J., Pelouard, J., Collin, S., 2011b. λ^3/1000 plasmonic nanocavities for biosensing fabricated by soft UV nanoimprint lithography. Nano Lett. 11, 3557–3563. https://doi.org/10.1021/nl201004c.

Chabot, V., Cuerrier, C.M., Escher, E., Aimez, V., Grandbois, M., Charette, P.G., 2009. Biosensing based on surface plasmon resonance and living cells. Biosens. Bioelectron. 24, 1667–1673.

Chabot, V., Miron, Y., Charette, P.G., Grandbois, M., 2013. Identification of the molecular mechanisms in cellular processes that elicit a surface plasmon resonance (SPR) response using simultaneous surface plasmon-enhanced fluorescence (SPEF) microscopy. Biosens. Bioelectron. 50, 125–131. https://doi.org/10.1016/j.bios.2013.06.018.

Chabot, V., Miron, Y., Grandbois, M., Charette, P.G., 2012. Long range surface plasmon resonance for increased sensitivity in living cell biosensing through greater probing depth. Sensor. Actuator. B Chem. 174, 94–101. https://doi.org/10.1016/j.snb.2012.08.028.

Coughlin, S.R., 2000. Thrombin signalling and protease-activated receptors. Nature 407, 258–264. https://doi.org/10.1038/35025229.

Cuerrier, C.M., Chabot, V., Vigneux, S., Aimez, V., Escher, E., Gobeil, F., Charette, P.G., Grandbois, M., 2008. Surface plasmon resonance monitoring of cell monolayer integrity: implication of signaling pathways involved in actin-driven morphological remodeling. Cell. Mol. Bioeng. 1, 229–239. https://doi.org/10.1007/s12195-008-0028-4.

Dalby, M.J., Giannaras, D., Riehle, M.O., Gadegaard, N., Affrossman, S., Curtis, A.S.G., 2004. Rapid fibroblast adhesion to 27nm high polymer demixed nano-topography. Biomaterials 25, 77–83. https://doi.org/10.1016/S0142-9612(03)00475-7.

de Bruijn, H.E., Kooyman, R.P.H., Greve, J., 1993. Surface plasmon resonance microscopy: improvement of the resolution by rotation of the object. Appl. Opt. 32, 2426–2430. https://doi.org/10.1364/AO.32.002426.

Fang, Y., 2011. Label-free biosensors for cell biology. Int. J. Electrochem. 2011, 1–16. https://doi.org/10.4061/2011/460850.

Fang, Y., Ferrie, A.M., Fontaine, N.H., Mauro, J., Balakrishnan, J., 2006. Resonant waveguide grating biosensor for living cell sensing. Biophys. J. 91, 1925–1940. https://doi.org/10.1529/biophysj.105.077818.

Fang, Y., Frutos, A., Verklereen, R., 2008. Label-free cell-based assays for GPCR screening. Comb. Chem. High Throughput Screen. 11, 357–369. https://doi.org/10.2174/138620708784534789.

Ferrie, A.M., Wu, Q., Fang, Y., 2010. Resonant waveguide grating imager for live cell sensing. Appl. Phys. Lett. 97, 223704. https://doi.org/10.1063/1.3522894.

Giaever, I., Keese, C.R., 1993. A morphological biosensor for mammalian cells. Nature 366, 591–592. https://doi.org/10.1038/366591a0.

Giebel, K.-F., Bechinger, C., Herminghaus, S., Riedel, M., Leiderer, P., Weiland, U., Bastmeyer, M., 1999. Imaging of cell/substrate contacts of living cells with surface plasmon resonance microscopy. Biophys. J. 76, 509–516. https://doi.org/10.1016/S0006-3495(99)77219-X.

Goedhart, J., Gadella, T.W.J., 2009. Fluorescence resonance energy transfer imaging of PKC signalling in living cells using genetically encoded fluorescent probes. J. R. Soc. Interface 6. https://doi.org/10.1098/rsif.2008.0340.focus.

He, R.-Y., Su, Y.-D., Cho, K.-C., Lin, C.-Y., Chang, N.-S., Chang, C.-H., Chen, S.-J., 2009. Surface plasmon-enhanced two-photon fluorescence microscopy for live cell membrane imaging. Optic Express 17, 5987. https://doi.org/10.1364/OE.17.005987.

Howe, C.L., Webb, K.F., Abayzeed, S.A., Anderson, D.J., Denning, C., Russell, N.A., 2019. Surface plasmon resonance imaging of excitable cells. J. Phys. Appl. Phys. 52, 104001. https://doi.org/10.1088/1361-6463/aaf849.

Huang, B., Yu, F., Zare, R.N., 2007. Surface plasmon resonance imaging using a high numerical aperture microscope objective. Anal. Chem. 79, 2979–2983. https://doi.org/10.1021/ac062284x.

Kreysing, E., Hassani, H., Hampe, N., Offenhäusser, A., 2018. Nanometer-resolved mapping of cell–substrate distances of contracting cardiomyocytes using surface plasmon resonance microscopy. ACS Nano 12, 8934–8942. https://doi.org/10.1021/acsnano.8b01396.

Liebermann, T., Knoll, W., 2000. Surface-plasmon field-enhanced fluorescence spectroscopy. Colloids Surf. Physicochem. Eng. Asp. 171, 115–130. https://doi.org/10.1016/S0927-7757(99)00550-6.

Loesberg, W., Teriet, J., Vandelft, F., Schon, P., Figdor, C., Speller, S., Vanloon, J., Walboomers, X., Jansen, J., 2007. The threshold at which substrate nanogroove dimensions may influence fibroblast alignment and adhesion. Biomaterials 28, 3944–3951. https://doi.org/10.1016/j.biomaterials.2007.05.030.

Maltais, J.-S., Denault, J.-B., Gendron, L., Grandbois, M., 2012. Label-free monitoring of apoptosis by surface plasmon resonance detection of morphological changes. Apoptosis 17, 916–925. https://doi.org/10.1007/s10495-012-0737-y.

McGuiness, R., 2007. Impedance-based cellular assay technologies: recent advances, future promise. Curr. Opin. Pharmacol. 7, 535–540. https://doi.org/10.1016/j.coph.2007.08.004.

Minami, T., Sugiyama, A., Wu, S.-Q., Abid, R., Kodama, T., Aird, W.C., 2004. Thrombin and phenotypic modulation of the endothelium. Arterioscler. Thromb. Vasc. Biol. 24, 41–53. https://doi.org/10.1161/01.ATV.0000099880.09014.7D.

Ni, Q., Mehta, S., Zhang, J., 2018. Live-cell imaging of cell signaling using genetically encoded fluorescent reporters. FEBS J. 285, 203–219. https://doi.org/10.1111/febs.14134.

O'Brien, P.J., Prevost, N., Molino, M., Hollinger, M.K., Woolkalis, M.J., Woulfe, D.S., Brass, L.F., 2000. Thrombin responses in human endothelial cells: CONTRIBUTIONS

from receptors other than PAR1 include the transactivation OF PAR2 BY THROMBIN-CLEAVED PAR1. J. Biol. Chem. 275, 13502–13509. https://doi.org/10.1074/jbc.275.18.13502.

Opal, S.M., van der Poll, T., 2015. Endothelial barrier dysfunction in septic shock. J. Intern. Med. 277, 277–293. https://doi.org/10.1111/joim.12331.

Otsu, N., 1979. A threshold selection method from gray-level histograms. IEEE Trans. Syst. Man Cybern. 9, 62–66. https://doi.org/10.1109/TSMC.1979.4310076.

Pancrazio, J.J., Whelan, J.P., Borkholder, D.A., Ma, W., Stenger, D.A., 1999. Development and application of cell-based biosensors. Ann. Biomed. Eng. 27, 697–711.

Peterson, A.W., Halter, M., Tona, A., Bhadriraju, K., Plant, A.L., 2009. Surface plasmon resonance imaging of cells and surface-associated fibronectin. BMC Cell Biol. 10, 16. https://doi.org/10.1186/1471-2121-10-16.

Peterson, A.W., Halter, M., Tona, A., Plant, A.L., 2014. High resolution surface plasmon resonance imaging for single cells. BMC Cell Biol. 15, 35. https://doi.org/10.1186/1471-2121-15-35.

Peterson, A.W., Halter, M., Tona, A., Plant, A.L., Elliott, J.T., 2018. Mass measurements of focal adhesions in single cells using high resolution surface plasmon resonance microscopy. In: Plasmonics in Biology and Medicine XV. Presented at the Plasmonics in Biology and Medicine XV. International Society for Optics and Photonics, pp. 1050905. https://doi.org/10.1117/12.2290776.

Progatzky, F., Dallman, M.J., Lo Celso, C., 2013. From seeing to believing: labelling strategies for in vivo cell-tracking experiments. Interface Focus 3 20130001–20130001. https://doi.org/10.1098/rsfs.2013.0001.

Rabiet, M.-J., Plantier, J.-L., Rival, Y., Genoux, Y., Lampugnani, M.-G., Dejana, E., 1996. Thrombin-Induced increase in endothelial permeability is associated with changes in cell-to-cell junction organization. Arterioscler. Thromb. Vasc. Biol. 16, 488–496. https://doi.org/10.1161/01.ATV.16.3.488.

Sarkar, M., Besbes, M., Moreau, J., Bryche, J.-F., Olivéro, A., Barbillon, G., Coutrot, A.-L., Bartenlian, B., Canva, M., 2015. Hybrid plasmonic mode by resonant coupling of localized plasmons to propagating plasmons in a kretschmann configuration. ACS Photonics 2, 237–245. https://doi.org/10.1021/ph500351b.

Scott, C.W., Peters, M.F., 2010. Label-free whole-cell assays: expanding the scope of GPCR screening. Drug Discov. Today 15, 704–716. https://doi.org/10.1016/j.drudis.2010.06.008.

Skoog, S.A., Kumar, G., Narayan, R.J., Goering, P.L., 2018. Biological responses to immobilized microscale and nanoscale surface topographies. Pharmacol. Ther. 182, 33–55. https://doi.org/10.1016/j.pharmthera.2017.07.009.

Söllradl, T., Banville, F.A., Chabot, V., Canva, M., Grandbois, M., Charette, P.G., 2017. Metal clad waveguide (MCWG) based imaging using a high numerical aperture microscope objective. Optic Express 25, 1666–1679. https://doi.org/10.1364/OE.25.001666.

Söllradl, T., Banville, F.A., Fröhlich, U., Canva, M., Charette, P.G., Grandbois, M., 2018a. Label-free visualization and quantification of single cell signaling activity using metal-clad waveguide (MCWG)-based microscopy. Biosens. Bioelectron. 100, 429–436. https://doi.org/10.1016/j.bios.2017.09.002.

Söllradl, T., Chabot, K., Fröhlich, U., Canva, M., Charette, P.G., Grandbois, M., 2018b. Monitoring individual cell-signaling activity using combined metal-clad waveguide and surface-enhanced fluorescence imaging. Analyst 143, 5559–5567. https://doi.org/10.1039/C8AN00911B.

Somekh, M.G., Liu, S.G., Velinov, T.S., See, C.W., 2000. High-resolution scanning surface-plasmon microscopy. Appl. Opt. 39, 6279–6287. https://doi.org/10.1364/AO.39.006279.

Son, T., Seo, J., Choi, I.-H., Kim, D., 2017. Label-free quantification of cell-to-substrate separation by surface plasmon resonance microscopy. Optic Commun. https://doi.org/10.1016/j.optcom.2017.10.001.

Toma, K., Kano, H., Offenhäusser, A., 2014. Label-free measurement of cell–electrode cleft gap distance with high spatial resolution surface plasmon microscopy. ACS Nano 8, 12612–12619. https://doi.org/10.1021/nn505521e.

Troyanovsky, B., Alvarez, D.F., King, J.A., Schaphorst, K.L., 2008. Thrombin enhances the barrier function of rat microvascular endothelium in a PAR-1-dependent manner. Am. J. Physiol. Lung Cell Mol. Physiol. 294, L266–L275. https://doi.org/10.1152/ajplung.00107.2007.

van der Heijden, M., van Nieuw Amerongen, G.P., van Bezu, J., Paul, M.A., Groeneveld, A.B.J., van Hinsbergh, V.W.M., 2011. Opposing effects of the angiopoietins on the thrombin-induced permeability of human pulmonary microvascular endothelial cells. PLoS One 6, e23448. https://doi.org/10.1371/journal.pone.0023448.

Vouret-Craviari, V., Boquet, P., Pouysségur, J., Van Obberghen-Schilling, E., 1998. Regulation of the actin cytoskeleton by thrombin in human endothelial cells: role of rho proteins in endothelial barrier function. Mol. Biol. Cell 9, 2639–2653. https://doi.org/10.1091/mbc.9.9.2639.

Wang, W., Wang, S., Liu, Q., Wu, J., Tao, N., 2012. Mapping single-cell–substrate interactions by surface plasmon resonance microscopy. Langmuir 28, 13373–13379. https://doi.org/10.1021/la301712h.

Watanabe, K., Matsuura, K., Kawata, F., Nagata, K., Ning, J., Kano, H., 2012. Scanning and non-scanning surface plasmon microscopy to observe cell adhesion sites. Biomed. Opt. Express 3, 354–359. https://doi.org/10.1364/BOE.3.000354.

Wei, S.-C., Yang, P.-T., Wu, T.-H., Lu, Y.-L., Gu, F., Sung, K.-B., Lin, C.-W., 2015. Characteristic investigation of scanning surface plasmon microscopy for nucleotide functionalized nanoarray. Optic Express 23 (20104). https://doi.org/10.1364/OE.23.020104.

Yeatman, E.M., 1996. Resolution and sensitivity in surface plasmon microscopy and sensing. Biosens. Bioelectron. 11, 635–649. https://doi.org/10.1016/0956-5663(96)83298-2.